WPMST1-CPR(17) 16979

E. Thoren et al.

Melt layer motion simulations with thermionic current constraints for an exposed tungsten edge in ASDEX Upgrade

Preprint of Paper to be submitted for publication in Proceeding of 16th International Conference on Plasma-Facing Materials and Components for Fusion Applications

This work has been carried out within the framework of the EUROfusion Consortium and has received funding from the Euratom research and training programme 2014-2018 under grant agreement No 633053. The views and opinions expressed herein do not necessarily reflect those of the European Commission.

Melt layer motion simulations with emission current constraints for an exposed tungsten edge in ASDEX Upgrade

E. Thorén[1], B. Bazylev[2], S. Ratynskaia[1], P. Tolias[1], K. Krieger[3], R. A. Pitts[4], S. Pestchanyi[2], M. Komm[5], B. Sieglin[3], the EUROfusion MST1 Team‡ and the ASDEX Upgrade Team[3]

[1]KTH Royal Institute of Technology, SE-10044 Stockholm, Sweden
[2]Karlsruhe Institute of Technology, P.O. Box 3640, D-76021 Karlsruhe, Germany
[3]Max-Planck-Institut für Plasmaphysik, 85748 Garching b. München, Germany
[4]ITER Organization, Route de Vinon-sur-Verdon, CS 90 046, 13067 St. Paul Lez Durance, France
[5]Institute of Plasma Physics CAS, Za Slovankou 3, 182 00 Prague 8, Czech Republic

E-mail: emitho@kth.se

Abstract. Simulations of recent ASDEX Upgrade experiments on transient-induced melting of a tungsten leading edge during ELMing H-mode are performed with the melt motion code MEMOS 3D. The description of the space-charge limited regime of thermionic emission, the mechanism responsible for the replacement current driving melt motion, has been updated in the code. The effect of non-periodic aspects of the spatio-temporal heat flux in the temperature distribution and melt characteristics as well as the importance of current limitation are investigated. Results are compared with the experimental observations of emission current and melt profile.

1. Introduction

Unsuccessfully mitigated edge localized modes (ELMs) can cause transient tungsten (W) melting, which is a primary concern for ITER [1]. Macroscopic motion of the molten W driven by electromagnetic forces or pressure gradients can lead to large-scale erosion which compromises the power handling capabilities of the local plasma-facing components (PFCs), whereas the rapid growth of hydrodynamic instabilities can lead to droplet ejection which may compromise plasma performance. As a consequence,

‡ See the author list of "Overview of progress in European Medium Sized Tokamaks towards an integrated plasma-edge/wall solution" by H. Meyer *et al.*, to be published in the Nuclear Fusion Special issue: Overview and Summary Reports from the 26th Fusion Energy Conference (Kyoto, Japan, 17-22 October 2016)

dedicated experiments have been designed in current devices against which simulation tools being used to assess the consequences of melting on ITER can be tested.

This work is focused on simulations using the MEMOS 3D melt motion code [3] of recent ASDEX Upgrade (AUG) experiments on repetitive transient melting of W during ELMing H-mode [2]. A W sample was exposed at the outer divertor target to Type 1 ELMing H-mode discharges producing transient parallel power flux densities of $\sim 1\,\mathrm{GW/m^2}$ over ms timescales at a frequency of ca 70 Hz. The W sample design is very similar to that employed in previous JET experiments [4] and provides a leading edge of 1 mm height nearly perpendicular to the magnetic field lines arriving at glancing angle to the target surface. A key enhancement with respect to the JET experiment is the electrical isolation of the sample and hence a capability to measure the total current flowing through the sample, providing an important constraint for the simulations. However, unlike in the JET experiment, no direct top surface IR measurements of the loaded sample are available for these ASDEX Upgrade exposures.

Following a brief presentation of the experimental conditions and some updates of the MEMOS 3D code mainly concerning the modelling of space-charge limited thermionic emission [5], we present a comparison between the total measured current and the computed thermionic current both for coherently averaged and raw (corrected for IR artifacts) ELM plasma heat flux profiles. The effect of non-periodic aspects of the spatio-temporal ELM heat flux as well as the role of space-charge limitation are investigated. Melt characteristics such as the poloidal extent, pool depth and build-up are calculated for the two heat load scenarios and compared with the experiment.

2. Experimental background and input

The AUG experiments on transient tungsten melting are described in detail in Ref.[2]. Both leading edge and sloped lamellae were exposed for a gradually increased duration in order to avoid the occurrence of bulk melting (namely melting also in-between ELMs). The discharges relevant for the transient melting of the leading edge are #33504, #33508 and #33509 - ELMing H-mode shots, all very similar in terms of input power and ELM characteristics, with B_t = - 2.5 T, I_p = 0.8 MA, P=7.5 MW [NBI], 2 MW [ECRH]. In this paper, we shall focus exclusively on discharge #33504. The input necessary for modelling was constructed from the heat flux derived for discharge #33511 (in which in fact the upper sloped sample was exposed) with an appropriate downward shift of the profile anchored to the measured position of the outer strike point (OSP) in pulse #33504.

Since the heat flux incident on the misaligned component was not directly measured, the heat flux distribution along the leading edge was evaluated by combining the optical approximation (in which particles are assumed to follow magnetic fields lines and any gyro-orbit motion is ignored) with the parallel heat flux deduced from outer target IR observations at a toroidal location distant from the sample [2]. Two representations of this heat flux, equivalent in terms of total energy delivered, have been employed in the

simulations; (i) an analytic fit of the spatio-temporal dependence of the ELM heat flux after coherent averaging that is repeated in the modelling for the duration at which the sample is loaded at the average ELM frequency of 67 Hz (ii) the raw heat flux profile and time-series after corrections have been applied to subtract IR artifacts due to reflections and bremsstrahlung, for details see Ref.[2]. This latter option is the only suitable way to account for spatio-temporal variations in the heat flux without having to introduce arbitrary stochastic fluctuations in the coherent ELM waveform. In Fig.1, the spatial and temporal profile of the coherent structure as well as several snapshots from the corrected raw data are displayed. The inter-ELM heat flux, derived from Langmuir probe data [2], is superposed on the coherent ELM (the IR data is not accurate in the inter-ELM phases). It is described by a spatial fit of the same nature as the ELM heat flux, with a peak value of $\sim 50\,\mathrm{MW/m^2}$, and is assumed to be constant in time.

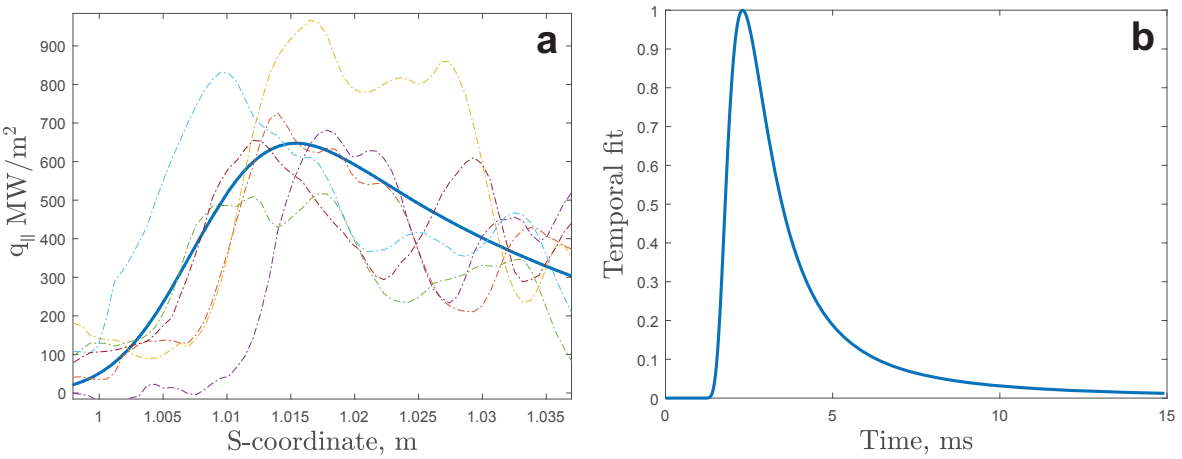

Figure 1. Spatial and temporal dependence of the ELM heat flux used as input to the MEMOS 3D modelling. (**a**) *Solid line:* Spatial distribution at the temporal maximum of the analytic fit to the coherent ELM. *Dashed lines:* Snapshots of the peak heat flux values extracted from the corrected raw data. (**b**) Temporal profile of the fitted coherent ELM. The spatio-temporal coherent averaged heat flux is obtained by multiplying the two profiles.

The measurements of the time-dependence of the total current flowing through the lamella to the grounded vessel (sampled at 200 kHz) constitute an important constraint for modelling. After subtraction of the current flowing through the flush mounted reference sample (originating mostly from thermoelectric currents flowing between the two divertor targets), the remaining current has been attributed to the replacement current triggered by thermionic emission from the heated surface [2].

3. Implementation in the MEMOS 3D code

In this section, we shall briefly describe the status of the MEMOS 3D code. In particular, we outline some recent updates relevant for the simulations reported here.

The temperature dependence of the *W thermophysical properties*, entering the heat transfer and hydrodynamic modules, have been updated according to the analytical formulas recommended in a recent survey [9]. The *vapour shielding* (but not vapour cooling) has been switched-off since the surface temperatures attained in the AUG experiments are relatively modest, with values typically not exceeding 4000 K.

The *boron-nitride (BN) substrate* which provides the electrical isolation of the W sample, being an efficient heat sink, has been introduced due to the necessity to closely mimic the heat pathways present in the experiments. The temperature dependence of the heat capacity and thermal conductivity of (high purity hot isostatically pressed) BN have been considered and a perfect thermal contact has been assumed at the W-BN boundary. The simulations revealed that for the short leading edge exposure simulated (the OSP is stable only for 0.5 s), heat diffusion to the BN substrate becomes significant after the OSP is shifted away from the lamella. Hence, below we only report results for a thermally insulated W lamella.

The treatment of *thermionic emission* in MEMOS 3D has been significantly updated. The nominal or unimpeded thermionic current density is described by the Richardson-Dushman formula $j_{\rm th}^{\rm RD}(T_{\rm s}) = A_{\rm eff} T_{\rm s}^2 \exp\left(-W_{\rm f}/kT_{\rm s}\right)$ where the values $W_{\rm f} = 4.55\,{\rm eV}$ and $A_{\rm eff} \simeq 60\,{\rm Acm^{-2}K^{-2}}$ have been employed for W, see Ref.[5] for justification. The current suppression due to space-charge effects has been quantified with the aid of systematic particle-in-cell simulations that have been carried out for the AUG inter- and intra-ELM plasma parameters with the 2D3V SPICE2 code [5, 6]. The PIC results for the space-charge limited current and the virtual cathode magnitude agreed exceptionally well with the predictions of an analytical theory for finite surface temperatures and cold ions [7], revealing only small systematic deviations [6]. The PIC limited current density was observed to closely follow a Child-Langmuir law that reads as $j_{\rm th}^{\rm lim} = 0.43 e n_{\rm e} v_{\rm Te}$, where $n_{\rm e}$ and $v_{\rm Te}$ are the plasma density and electron thermal velocity, respectively [6]. This relation can be transformed to an expression connecting the limited current with the parallel heat flux under the additional assumptions: (i) $T_{\rm i} = T_{\rm e}$ for the ion temperature, (ii) $c_{\rm s} = \sqrt{(T_{\rm e} + T_{\rm i})/m_{\rm i}}$ for the sound speed, (iii) $\gamma = 7$ for the sheath heat transmission coefficient, (iv) $n_{\rm e} = {\rm const.}$ implying that heat flux spatio-temporal variations are due to temperature variations. These lead to the simple expression $j_{\rm th}^{\rm lim}(q_\parallel) = 1.51 \times 10^{-4}\, q_\parallel^{1/3}$, where $q_\parallel$ denotes the parallel heat flux. Supplementing the Richardson-Dushman formula with the above limiting value, we simply have $j_{\rm th}(T_{\rm s}, q_\parallel) = \min\left\{j_{\rm th}^{\rm RD}(T_{\rm s}), j_{\rm th}^{\rm lim}(q_\parallel)\right\}$. Equivalently, denoting the solution of $j_{\rm th}^{\rm RD}(T_{\rm s}) = j_{\rm th}^{\rm lim}(q_\parallel)$ with $T_{\rm s}^{\rm lim}(q_\parallel)$, we end up with

$$j_{\rm th}(T_{\rm s}, q_\parallel) = \begin{cases} A_{\rm eff} T_{\rm s}^2 \exp\left(-\dfrac{W_{\rm f}}{kT_{\rm s}}\right) & T_{\rm s} \le T_{\rm s}^{\rm lim}(q_\parallel)\,, \\ 1.51 \times 10^{-4}\, q_\parallel^{1/3} & T_{\rm s} \ge T_{\rm s}^{\rm lim}(q_\parallel)\,. \end{cases} \tag{1}$$

The obvious advantage of this treatment is that it enables us to directly reflect the effect of the spatio-temporal heat flux variations in the thermionic current, rather than introducing suppression factors for a restricted combination of plasma parameters. Note

that thermionic emission contributes to cooling with an energy release of $2kT_\mathrm{s} + W_\mathrm{f}$ per emitted electron [5, 8]. For a comparison with the total current versus time measurements, Eq.(1) is determined for every surface element at each time instant and integrated over the plasma-facing sample surface, *i.e.* $I_\mathrm{th}(t) = \int j_\mathrm{th}[T_\mathrm{s}(S,t), q_\parallel(S,t)]dS$.

The physics of the *replacement current density* that is responsible for the $\boldsymbol{J}\times\boldsymbol{B}$ force driving the melt motion [1] has been revisited. This current density flows through the **bulk** of the lamella in order to replenish the thermionic electrons emitted at the plasma-facing **surface**. The Lorentz force density acting on each volume element of the melt layer is determined by the magnetic field $\boldsymbol{B}$ and the local replacement current density $\boldsymbol{J}$, with two contributions at each spatial direction. The dominant force contribution is along the poloidal direction; it is the source of the experimentally observed poloidal melt motion and stems from the radial current density component J_eff and toroidal magnetic field component.

The computation of the replacement current at each point of the melt layer is a non-trivial issue, even when considering the steady state problem in the absence of magnetic fields. The boundary value problem consists of the current continuity equation $\nabla\cdot\boldsymbol{J} = 0$, the irrotational constraint for the electrostatic field combined with Ohm's law (ρ_el is the dc resistivity) $\rho_\mathrm{el}(\nabla\times\boldsymbol{J})+(\nabla\rho_\mathrm{el})\times\boldsymbol{J} = 0$ and is complemented by appropriate boundary conditions that include thermionic emission as a current sink. Numerical solutions have been obtained with the finite element method (COMSOL Multiphysics) and revealed details of the current paths, the relative magnitude and spatial dependence of the different $\boldsymbol{J}\times\boldsymbol{B}$ components acting on the melt layer. For brevity these results are not, however, presented here. For simplicity, only the upper limit of the dominant component has been considered; it is assumed that at each fluid element J_eff is equal to the current density emitted from the surface element directly above in the direction perpendicular to the plasma-facing edge.

4. Modelling results and discussion

In #33504, at $t = 3.3\,\mathrm{s}$ the OSP was shifted down to its stationary position on the sample ($s_0 = 1.008\,\mathrm{m}$) and was maintained there until $t = 3.8\,\mathrm{s}$, when it was shifted upwards off the lamella. Fig.2 compares the measured and the computed currents for MEMOS 3D runs with coherent averaged (a) and corrected raw (b) heat fluxes. Unfortunately, the saturation level of the measurement system is reached during the ELM spikes that fall in the $3.65 - 3.95\,\mathrm{s}$ span and the recorded current is truncated, hindering comparison with simulations in this time interval. The initial phase of the experimental data reveals peaks nearly from the start of the OSP sweep to the sample, which cannot be reproduced even by imposing large uncertainty margins in the heat flux magnitude and the OSP timing. In particular, for the coherent ELM, 0.3 s from the start of the OSP sweep are required for the inter-ELM surface temperature to exceed 2000 K at any point. The ELM-induced temperature excursions are $\sim 1000\,\mathrm{K}$ and thus 3000 K is not exceeded until after 3.3 s, which is the lowest surface temperature required

for the exposed area to emit 5 A solely by thermionic emission. However, this value is rapidly exceeded in measurements and the baseline indicates a relaxed inter-ELM surface temperature in excess of 3000 K as early as 3.3 s into the exposure. Such a significant discrepancy indicates that the measured current cannot be solely attributed to thermionic emission and that a current source of different nature should be present in the signal. In fact, in the latest AUG experiments, where current measurements were accompanied by simultaneous surface temperature measurements [10], significant current peaks were already detected for temperatures below $1500 - 2000$ K. The origin of this additional current source is presently not understood.

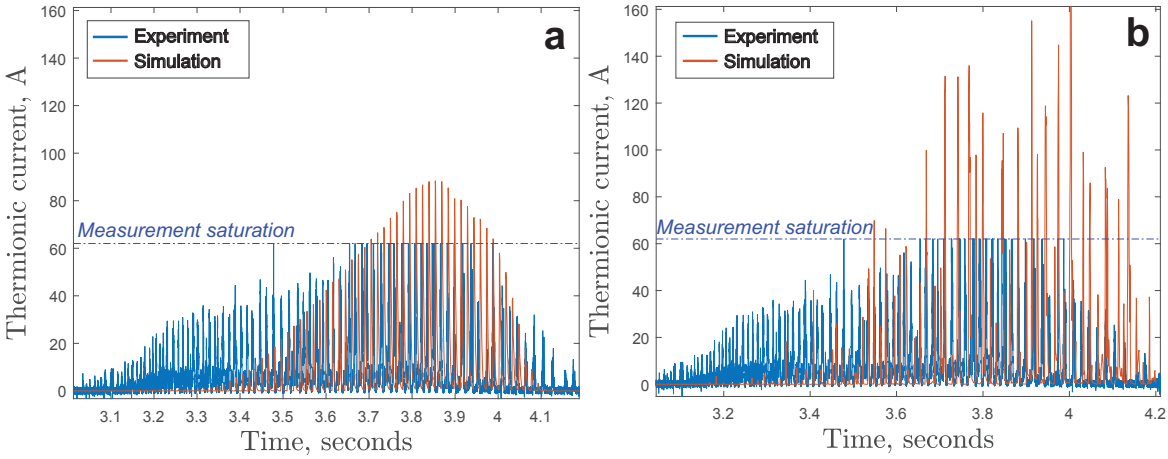

Figure 2. Comparison of the temporal dependence of the integrated thermionic emission current from MEMOS simulations (red) with the experimental current measurements (blue), for the leading edge exposure in shot #33504. Simulations employing the (a) coherent averaged heat flux and (b) corrected raw heat flux data.

The computed thermionic current reproduces the temporal behaviour and lies within an order of magnitude of the measured current, but none of the simulations approach the measurements quantitatively. This is not caused solely by the unknown contribution of the additional current source, but also because the coherent flux averages out some important characteristics; it repeatedly strikes the same position with identical magnitude so that the emerging thermionic current envelope is monotonically increasing (due to the base temperature increase on which nearly constant ELM temperature excursions are superimposed). On the other hand, as clearly illustrated in Fig.1, the individual ELMs can have significant variations not only in the heat flux profile and the position of its maximum but also in the energy delivered. These characteristics allow the reproduction of variations present in the measured signal, namely occasional "violent" current bursts and followed by "quiescent" periods. However, a one-to-one correspondence is unfeasible since the heat flux data are from another discharge and are measured at a toroidal location very far from the W sample (ELMs are inherently toroidally asymmetric). These differences are also reflected in the spatio-temporal behaviour of the surface temperature and melt depth, see below.

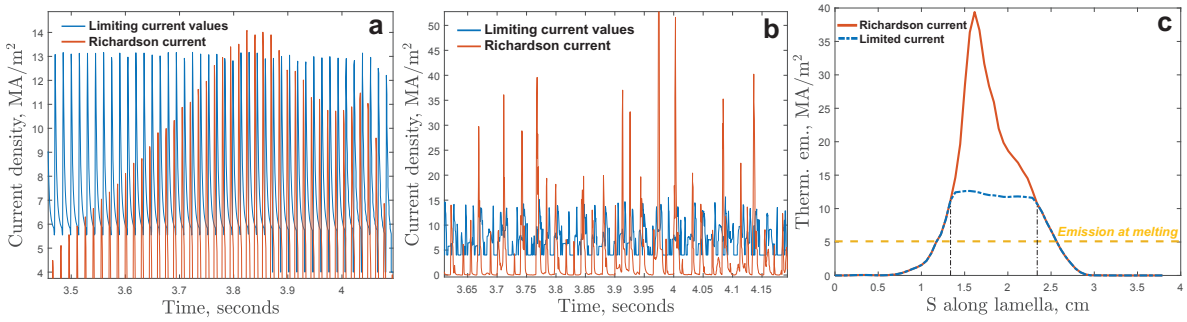

Figure 3. The unimpeded thermionic current density $j_{\rm th}^{\rm RD}(T_{\rm s})$ according to the Richardson-Dushman formula (red) *for the point of maximum temperature* on the plasma-facing edge and the heat-flux dependent limiting current density value $j_{\rm th}^{\rm lim}(q_{\parallel})$. Simulations with (a) coherent averaged and (b) corrected raw heat flux data. (c) Snapshot of a large event from the corrected raw heat flux runs quantifying the relative contributions of the unimpeded current (blue) and the limited current (red), the vertical lines indicate entry to the space-charge limited regime.

To attribute the measured total current to thermionic emission, a comparison with the Richardson current is usually performed using oversimplified assumptions for the emitting area and the surface temperature, typically considered equal to the molten region and the melting point or above, respectively [11, 12]. With the simulation results we are in position to identify the contributions to the total current from different regions of the wetted area. Fig.3 shows the limiting current values $j_{\rm th}^{\rm lim}(q_{\parallel})$ (in blue) and the unimpeded thermionic current $j_{\rm th}^{\rm RD}(T_{\rm s})$ according to the Richardson-Dushman formula (in red) for the coherent (a) and corrected raw heat fluxes (b). Note that, owing to cooling by thermionic emission, for the comparison to be meaningful, $j_{\rm th}^{\rm RD}(T_{\rm s})$ was calculated for the surface temperature profiles obtained from runs with limited thermionic emission following Eq.(1). Fig.3a shows that for the coherent flux, even though from 3.7 s and onwards part of wetted area is molten, the limited regime is only entered in a few instances. In contrast, Fig.3b reveals that for the corrected raw flux a significant number of (but not all) ELMs bring thermionic emission into the limited regime (with large, factor of 2-3 differences between the unimpeded and limiting values). In a spatial snapshot of one of the larger events, as in Fig.3c, the total current is observed to comprise of two comparable contributions; from the area with temperature exceeding the critical value for a given heat flux and thus emitting at the limiting value (between the vertical lines, under the red curve) and from the remaining area emitting the unimpeded Richardson current (wings, left and right of the vertical lines).

The necessity to include the stochastic character of the spatio-temporal behaviour of the ELM heat fluxes can be further highlighted by comparing the basic figures-of-merit of the molten area, namely the poloidal extension and the molten depth. The bottom panel of Fig.4 illustrates the melt pool formed during each ELM for coherent averaged (b) and corrected raw heat fluxes (d), starting from 3.7 s, when the base temperature first approaches ~ 3000 K and melting becomes significant. Prior to comparing with the

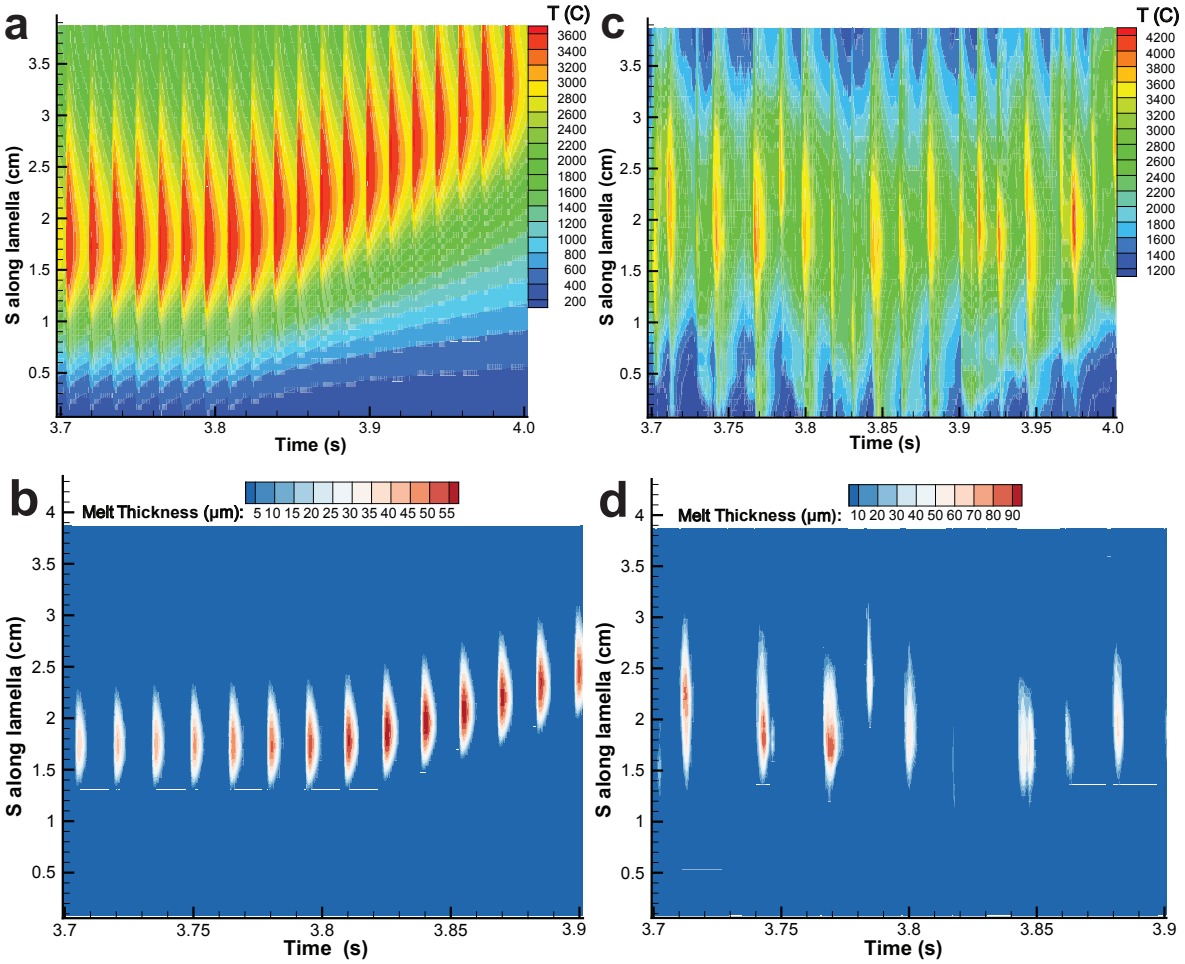

Figure 4. Temporal dependence of the poloidal profile of the surface temperature (upper row) and the thickness of the melt pool (lower row) at *the uppermost edge* of the exposed surface. Simulations with (a,b) coherent averaged and (c,d) corrected raw heat flux data.

experiment, we should emphasize that surface analysis was carried out post-mortem and documented the cumulative effect of all discharges - #33504 (simulated here), #33508 and #33509. It is also worth noting that the last exposure was appreciably longer: the OSP was held on the sample for 1.1 s in contrast to the 0.5 s simulated here. The poloidal melt extent and melt depth range respectively within $0.9 - 1.1\,\mathrm{cm}$ and $40 - 55\,\mu\mathrm{m}$ for the coherent ELM heat flux and $0.8 - 1.7\,\mathrm{cm}$ and $40 - 90\,\mu\mathrm{m}$ for the corrected raw ELM heat flux. The experimental data yield $\sim 1.5\,\mathrm{cm}$ for the poloidal extent as deduced from the final erosion profile of the lamella and $\sim 100\,\mu\mathrm{m}$ for the pool depth as deduced from SEM images of the re-solidified melt [2]. Finally, the displaced melt volume (the "build-up") is $0.4\,\mathrm{mm}^3$ and $0.7\,\mathrm{mm}^3$ for the coherent and corrected raw ELMs, respectively. These numbers are to be compared with the experimentally observed displaced molten volume, $\sim 7\,\mathrm{mm}^3$, obtained from the final erosion profile [2]. Since melt build-up does not scale linearly with the exposure time due to the evolution of the base temperature,

resulting in more efficient melting (deeper melt pools and stronger thermionic emission) at later stages, the main contribution to the experimental value is due to the last longest exposure. Indeed, longer runs, where the stable OSP duration was simply extended, lend full support to such interpretation.

In conclusion, the scaling of limiting current with the heat flux as given by Eq.(1) results in an intimate coupling with details of the spatio-temporal behaviour of the heat flux. An aperiodic temporal pattern of the heat flux, including temporarily sharper ELMs, implies inhibited conduction and hence higher surface temperatures. The latter leads to a more efficient passage of the thermionic current into the limited regime. Hence, the whole interplay between the limited current and melt motion is different from the case of a periodic coherent heat load. Variations in the spatial heat flux density profile have a dual effect as well; they prevent overheating of the same spot by distributing the heat in different location at each ELM but also allow for higher local energy density. The latter again implies more efficient switching to the limited regime.

Acknowledgments

This work has been carried out within the framework of the EUROfusion Consortium and has received funding from the Euratom research and training programme 2014-2018 under grant agreement No 633053. Work performed under WP MST1. The views and opinions expressed herein do not necessarily reflect those of the ITER Organization or of the European Commission. ITER is the nuclear facility INB 174.

[1] Pitts R A, Bardin S, Bazylev B *et al.* 2017 Physics conclusions in support of ITER W divertor monoblock shaping *Nucl. Mat. Energy* http://dx.doi.org/10.1016/j.nme.2017.03.005
[2] Krieger K, Coenen J W, Matthews G F *et al.* 2017 *Nucl. Fusion* (submitted)
[3] Bazylev B, Janeschitz G, Landman I *et al.* 2009 *J. Nucl. Mater.* **390-391** 810
[4] Coenen J W, Arnoux G, Bazylev B, Matthews G F *et al.* 2015 *Nucl. Fusion* **55** 023010
[5] Komm M, Ratynskaia S, Tolias P *et al.* 2017 *Plasma Phys Cont Fusion* (submitted)
[6] Komm M, Tolias P, Ratynskaia S *et al.* 2017 *Phys. Scr.* (these proceedings)
[7] Takamura S, Ohno N, Ye M Y and Kuwabara T 2004 *Contrib. Plasma Phys.* **44** 126
[8] Herring C, and Nichols M H 1949 *Rev. Mod. Phys.* **21** 185
[9] Tolias P 2017 arXiv:1703.06302v1
[10] Krieger K, Sieglin B, Balden M *et al.* 2017 *Phys. Scr.* (these proceedings)
[11] Sergienko G, Bazylev B, Hirai T *et al.* 2007 *Phys. Scr.* **T128** 81
[12] Coenen J W, Philipps V, Brezinsek S *et al.* 2011 *Nucl. Fusion* **51** 083008